17

Cryoelectron Microscopy of Icosahedral Virus Particles

Wen Jiang and Wah Chiu

Summary

With the rapid progresses in both instrumentation and computing, it is increasingly straightforward and routine to determine the structures of icosahedral viruses to subnanometer resolutions (6–10 Å) by cryoelectron microscopy and image reconstruction. In this resolution range, secondary structure elements of protein subunits can be clearly discerned. Combining the three-dimensional density map and bioinformatics of the protein components, the folds of the virus capsid shell proteins can be derived. This chapter will describe the experimental and computational procedures that lead to subnanometer resolution structural determinations of icosahedral virus particles. In addition, we will describe how to extract useful structural information from the three-dimensional maps.

Key Words: Cryo-EM; cryoelectron microscopy; icosahedral virus; 3D reconstruction; subnanometer resolution; secondary structure elements; structural fitting

1. Introduction

Icosahedral virus particles were among the first biological specimen for which three-dimensional (3D) molecular structures have been solved using electron microscopy, image processing, and 3D reconstruction ***(1,2)***. Because of their large size, high symmetry, and availability in large quantities, icosahedral virus particles frequently have been studied structurally by single particle cryoelectron microscopy (cryo-EM). These studies, for example, the hepatitis B virus ***(3,4)***, herpes simplex type-1 capsid ***(5)***, and rice dwarf virus ***(6)***, have played and are continuing to play key roles in the development of cryo-EM technologies and in pushing for increasingly higher resolutions, accuracy, and throughput.

In recent years, we have seen significant progress in cryo-EM studies of icosahedral virus structures toward subnanometer resolutions (6–10 Å; Chiu et al. ***[7]***). At these resolutions, it is possible to discern the protein boundaries at most of the regions and allow the dissection of the assembly mechanisms of multiple components in the large virus capsid. Secondary structure elements (alpha helices and beta sheets) can also be discerned. The visualization of these

From: *Methods in Molecular Biology, vol. 369*
Electron Microscopy: Methods and Protocols, Second Edition
Edited by: J. Kuo © Humana Press Inc., Totowa, NJ

structural features not only validates the structures but also allows searching homologue protein fold using the spatial information of (alpha helices and beta sheets; Jiang et al. ***[8]***). By integrating bioinformatics, homology modeling, the subnanometer resolution structures, and the identified secondary structure elements, atomic models can be built for the protein subunits ***(9)***. This progress was made possible by advances in all aspects of cryo-EM study: instrumentation, image acquisition, image processing/3D reconstruction software, computing resource, and structural analysis and interpretation tools. The following sections will describe each of these steps and discuss the protocols in the order that parallels the pipeline for a typical cryo-EM study.

2. Materials

There are many different types of equipment needed for successful cryo-EM imaging and 3D reconstruction of icosahedral viruses. Examples of the major equipments and their suppliers used in our Center are listed:

1. Quantifoil® R2/2 grids (Quantifoil Micro Tools GmbH, Germany).
2. Emitech glow discharger (http://www.emitech.co.uk).
3. Vitrobot™ (http://www.vitrobot.com) or equivalent freeze plunger (http://www.gatan.com/holders/cryoplunge.html).
4. Gatan or Oxford cryo-holder and cryo-transfer station (http://www.gatan.com).
5. JEOL or FEI 200-300kV electron microscopes with LaB_6 or field emission gun with cryo-stage and low dose kit.
6. Gatan or Tietz 4K × 4K CCD camera for direct digital recording.
7. Kodak SO163 photographic films and darkroom.
8. Nikon CoolScan 9000ED scanner or equivalent scanner.
9. Tweezers, liquid N_2 tank, and other small accessories for cryo-EM imaging.
10. Computer cluster for image processing (10–20 CPUs of current Intel Xeon or AMD Athlon/Opetron running at 1–3 GHz with 1–2 GB memory per CPU).
11. Graphical workstation for image and 3D map visualization.
12. Image processing software: EMAN ***(10)*** and SAVR ***(11)*** (http://ncmi.bcm.edu/software). There are other software packages suitable for this task. In this article, we will refer to the programs in the freely available EMAN or SAVR software packages if not otherwise specified.
13. 3D Visualization software: Amira™ (http://www.amiravis.com) or Chimera (http://www.cgl.ucsf.edu/chimera).

3. Methods

3.1. Data Collection

3.1.1. Specimen Preparation

The virus particles should be purified to homogeneity, usually by gradient centrifugation followed by thorough dialysis. The final buffer solutions should keep the virus particles stable. In general, the preferred buffer has <300 m*M*

salt. Detergent and sucrose/glycerol should be avoided. Buffers with a smaller pH dependence on temperature, such as phosphate-buffered saline instead of Tris buffer, are preferred to minimize the pH change from the approx 200° temperature decrease during sample freezing ***(12)***. The optimal concentration of each virus sample is dependent on the sample and buffer, but a good starting point is at approx 10^{12} particles/mL or approx 1 mg/mL in general. At this concentration, a total sample volume of 50 to 200 µL generally is adequate for collecting a sufficient number of images for a subnanometer resolution 3D reconstruction.

3.1.2. Sample Freezing

The goal is to preserve the virus particles in a thin layer of vitreous ice on a holey grid. Flash freezing of the sample is required to prevent formation of ice crystals that can damage the virus particles ***(13,14)***.

1. Holey grids: 400 mesh copper grids coated with a thin layer of carbon film with 2- to 4-µm diameter holes. Commercial Quantifoil grids or home-made holey grids ***(15)*** can be used. The grids should be thoroughly cleaned using organic solvents, such as acetone, to remove residual plastics that can cause charging and interfere with image quality. The grids also typically are glow discharged before use to clean the grid surface and to make the carbon film surface more hydrophilic so that the aqueous biological sample will stick to the grid better. The optimal strength and duration of the glow discharging varies with the grids and the samples, and needs to be determined for each study. A reasonable starting condition is approx 20 s, with a current of 20 mA using an Emitech glow discharger. Note that gloves should be worn when handling the grids. The grids should be handled very gently to avoid bending or other deformations.
2. Plunge freezing: A homemade gravity-driven plunger has been used successfully ***(16)***. However, a more elaborate plunge freezer, the Vitrobot, with environmental chamber and computer control capability is also commercially available. When using these freezing apparatuses, a sharp-tipped tweezer with a holey grid clamped at the edge is held by a vertically movable rod. A small volume of sample solution (3–5 µL) is pipetted on the surface of the grid and excess solution is then blotted away for a few seconds using filter paper (*see* **Note 1**). After blotting, the grid is plunged into a receiving well with ethane slush cooled by liquid N_2. Rapid plunging, driven either by gravity or pneumatic pressure, is essential to ensure a fast cooling rate to form a vitreous ice layer embedding the particles. A slower cooling rate will result in the formation of ice crystals which may damage the specimen. The frozen grid is placed into a transfer grid box for storage in a liquid N_2 dewar or tank for later imaging in the microscope.

3.1.3. Imaging

Acquisition of high-quality images of the virus particles is the critical step to ensure a 3D reconstruction towards subnanometer resolutions. As the result

of instrument advances, this task can be routinely performed using modern electron microscopes.

1. Microscope: A 200- to 300-kV microscope with LaB_6 or field emission gun can be used. The microscope should have liquid nitrogen or helium cooled stage, cryotransfer system, anticontamination blades and low dose imaging kit. Microscopes with these accessories are available from many vendors, with the majority of installations from JEOL and FEI.
2. Cryotransfer of grid into the microscope column: A side entry Gatan or Oxford cryoholder typically is used. This type of holder has a dewar on the far end that can be filled with liquid N_2 to cool the holder tip (where the grid is located) via thermal coupling. The holder is inserted into a pre-cooled cryotransfer station where the holder tip is semi-immersed within a liquid nitrogen bath. The dewar of the cryoholder is filled with liquid nitrogen. When the tip of the cryoholder reaches −170°C, the frozen grid is transferred from its storage slot of the grid box to the grid-seat at the holder tip using a pre-cooled tweezer. A small clip or screw ring secures the grid firmly in place. With the grid shutter closed, the cryoholder is then retracted from the cryotransfer station and rapidly inserted into the pre-pumped airlock of the microscope column (*see* **Note 2**). After cryotransfer of a grid into the column, a short period of wait time (several minutes) is generally needed to allow the full recovery of the vacuum in the column and mechanical stability of the specimen stage before proceeding to data collection.
3. Image acquisition: The microscope needs to be aligned well to acquire high resolution images. Astigmatism should be corrected to a negligible amount by minimizing either the ellipticity of the power spectra at a small under-focus when using a CCD camera or by judging the image contrast at different focuses using a TV monitor or the microscope fluorescent screen. Smaller condenser apertures and suitable spot sizes should be used to increase the spatial coherence of the beam while still providing efficient beam brightness. A small objective aperture is used to maximize the image contrast but should be large enough not to cut off high frequency information.

   Low-dose imaging is used to minimize radiation damage of the specimen by the electron beam. A low magnification (5000X) or defocused diffraction mode and low-intensity beam is used for the search mode to survey the grid and identify areas suitable for imaging. A focused beam at the same magnification as used in the final imaging is used to adjust the defocus using an area adjacent to the area of interest. It is critical to record the image only when there is no apparent stage and specimen drift. For studies aiming at subnanometer resolutions, typically 4000 to 8000 particles are collected which can usually be accomplished with a few imaging sessions.

   The aforementioned search/focus/imaging cycle for the whole grid typically is performed manually by the user. However, semi or fully automated imaging is becoming available on the new generation microscopes using software packages such as JAMES ***(17)***, Leginon ***(18)***, AutoEM ***(19)***, or AutoEMation ***(20)***.

4. Recording medium: Traditionally, photographic films such as Kodak SO163 are the recording medium for cryo-EM images. The exposed negatives are developed for 12 minutes using full strength developer solution at 20°C and subsequently fixed. Alternatively, high-resolution CCD cameras with 4k × 4k pixels, such as the Gatan UltraScan™ 4000 and Tietz TemCam F415, have become available for 200- to 300-kV electron microscopes in recent years and have been shown to be capable of recording virus particle images that yield subnanometer resolution 3D reconstructions ***(17,21)***. Using a CCD provides several advantages over the use of photographic film for medium resolution reconstructions because: direct digitization eliminates the need for film development and subsequent digitization, water contamination in the electron microscope column is reduced due to the absence of photographic film, and image contrast is improved ***(17)***. CCD recording also simplifies the automated image collection protocol.
5. Imaging conditions: 50,000 to 60,000 magnifications typically are used with film as a recording medium, when targeting at subnanometer resolutions. However, higher microscope magnifications (60,000–80,000) are needed for CCD imaging due to the modulation transfer function characteristics of the current 4k CCD ***(17)***. Underfocuses in the range of 1 to 3 μm are good choices to minimize the signal decay at high resolutions but still maintain adequate image contrast for easy particle selection and orientation determination. The final image is usually taken using a total dose of <20 e/Å^2 on the sample typically in a 1 second exposure.
6. Digitization of images recorded on photographic films: Currently, the Nikon CoolScan 9000ED scanner (*see* **Note 3**) can be used to digitize the film at 6.35 μm/pixel for 3D reconstructions at subnanometer resolution ***(22)***. The drawback of the Nikon scanner is that only approx 90% of film width can be scanned and requires a modified film holder to clamp the film into the proper position. The quality of the scans needs to be checked periodically to ensure that the scanner works at top performance. The scanning parameters should also be adjusted so that the histograms of the scanned images will adequately sample the whole dynamic range (16 bit) of the scanner.
7. Digital sampling: Based on Shannon information theory, at least 2X spatial sampling is required to preserve the structural details at the intended resolutions. In practice, 3X sampling is generally needed. When targeting at subnanometer resolution (6–10 Å) 3D reconstructions, images should be sampled at 2 to 3.5 Å/pixel to satisfy this requirement. The practical approach is to use the above-suggested magnification for imaging and the scanning step sizes, and then average the data at 1.5 or 2X.

3.2. Preprocessing

Before actual image processing to determine the orientation of all particles, the following preprocessing tasks should be completed.

3.2.1. Image Screening

Cryo-EM images (*see* **Fig. 1**) are rarely 100% suitable for data processing for 3D structure determination. Many factors, such as ice contamination and

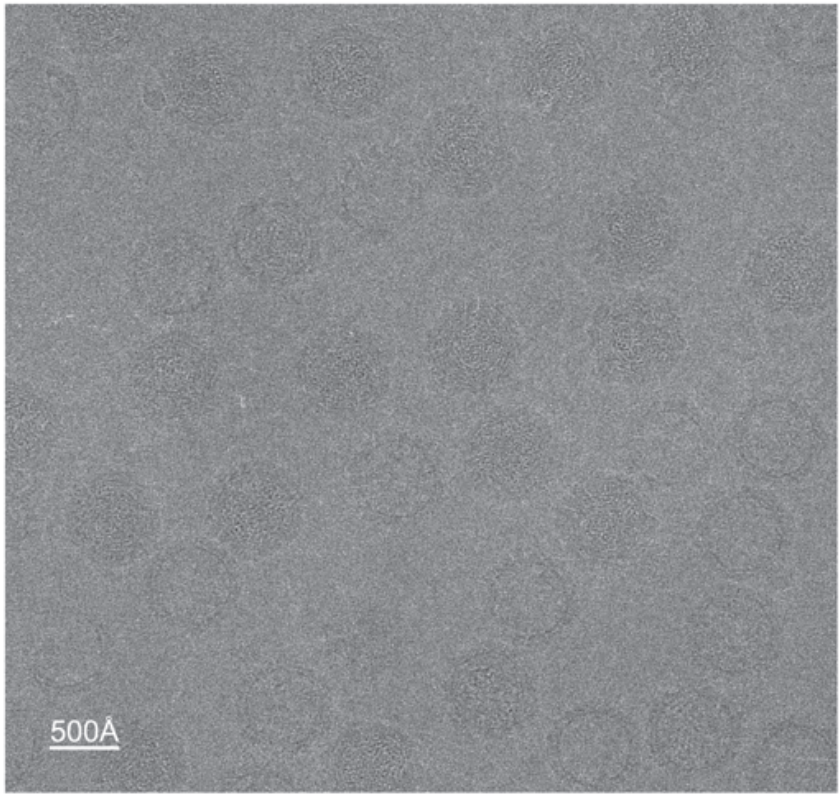

Fig. 1. A typical low-dose image of ice-embedded rice dwarf virus particles imaged at 2.1 μm underfocus on a JEM4000 electron microscope equipped with a Gatan liquid nitrogen cryoholder.

specimen drift, will render many images unusable. Visual inspection using the graphical programs *boxer* or *eman*, can be used to discard the images with too few particles, too much contamination or obvious charging/drift. The power spectra of the digital images should be inspected (using *ctfit*) to discard those without Thon rings at the targeted resolutions, those with obviously elongated Thon rings due to astigmatism, and those exhibiting anisotropic Thon rings caused by significant charging or drift (*see* **Fig. 2**).

3.2.2. Particle Selection

Individual good particles would be selected for the later image processing. Both manual and automated particle selection are available; however, in practice, combined manual screening post automatic selection is the best practical approach to ensure high quality selection.

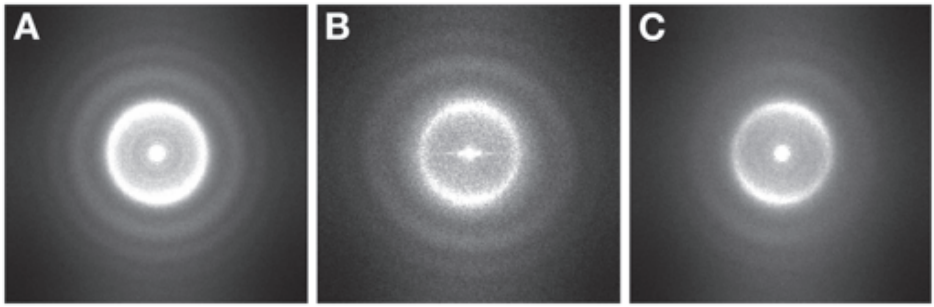

Fig. 2. Examples of power spectra of incoherent averages of virus particles with different image qualities. **(A)** good; **(B)** astigmatic; **(C)** drift.

1. Pre-filtering of images: because the purpose of particle selection is to mark the center position of selected particles, the fully sampled image is not necessary. In fact, prefiltered images by averaging and low-pass filtering can speed up particle selection by enhancing the visibility of the particles ***(23)*** and shrinking the number of pixels for rapid computation turnaround. Appropriate averaging and filtering could be performed using the *proc2d* program so that the shrunken particle diameter is about 80–100 pixels. The coordinates of the particles in the original fully sampled image are easily computed by multiplying the amount of averaging.
2. Automated selection: Many automated particle selection programs are available with a broad range of applicable sample types, selection accuracy and speed ***(24)***. Our preferred method for the spherical virus particle selection is the *ethan* program (http://www.cs.helsinki.fi/group/bimcom/spade) using the ring filter algorithm ***(25)***. It is fast (a few seconds per micrograph), nearly parameter free and has good selection accuracy (*see* **Fig. 3A**). The *ethan.py* program runs *ethan* and automatically handles the format conversions from/to EMAN conventions.
3. Manual screening: *ethan* also would select the particles on the carbon film area between the holes, nonparticle contaminations, or particles that are too crowded. Manual screening with the graphic program *boxer* could be used to discard those undesirable particles (*see* **Fig. 3B**).

3.2.3. CTF Parameter Determination

The images taken on an electron microscope are modulated by the contrast transfer function (CTF; *see* **Fig. 4A**) of the electron optical system and the experimental envelope functions ***(26–28)***. Because the modulations vary for different micrographs, it is critical to accurately determine the parameters for the CTF and envelope function for each micrographs or CCD frames. The determined parameters would be used in the image refinement/3D reconstruction steps.

Defocus is the primary parameter, which varies in each micrograph. It will dictate the frequency ranges in which phase flipping of the Fourier transform complex values must be made. In addition, the experimental B factor ***(29)*** needs to be corrected for the Fourier signal amplitudes during the 3D reconstruction.

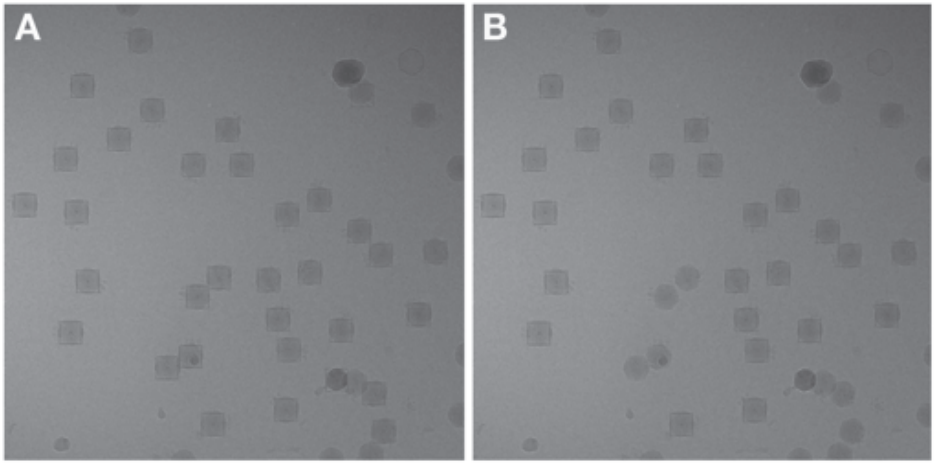

Fig. 3. Examples of particle selection. **(A)** automatically selected particles. **(B)** selected particles after manual screening.

The 2D power spectra of all particles within the same micrograph are incoherently averaged to generate the 2D power spectrum of each micrograph (using *proc2d fftavg* option or *ctfit*). Because the average power spectrum of a good image with minimal drift and astigmatism is essentially isotropic, the 2D power spectrum can be further rotationally averaged to generate a 1D power spectrum curve (using *ctfit*). The CTF fitting process in general is then performed with this 1D curve. It is essentially a curve fitting problem by adjusting the CTF parameters to match the predicted power spectra to the experimental power spectra.

Using *ctfit*, the noise background of the power spectra should first be fitted to touch the minima. The defocus and experimental B factor are then fitted by adjusting the corresponding slider controls in the GUI. A good fit will have the peak/minima positions aligned and the peak heights matched (*see* **Fig. 4B** and also **Note 4**).

Once the CTF parameters are fitted, the corresponding CTF and associated parameters should be recorded in the image headers of each particle. When the EMAN *refine* program is used for the image refinement, the particles should also be CTF phase corrected by flipping the phases in the frequency ranges where CTF amplitude is negative. Both operations can be performed using the program *applyctf* or *ctfit*.

3.3. 2D Image Alignment and 3D Reconstruction

The 3D reconstruction of icosahedral viruses was first introduced by Crowther et al. ***(1,2)***. There are numerous software packages such as Spider ***(30)***, IMAGIC ***(31)***, Frealign ***(32)***, PFT ***(33)***, XMIPP ***(34)***, IMIRS ***(35)***, SAVR ***(11)***, and EMAN

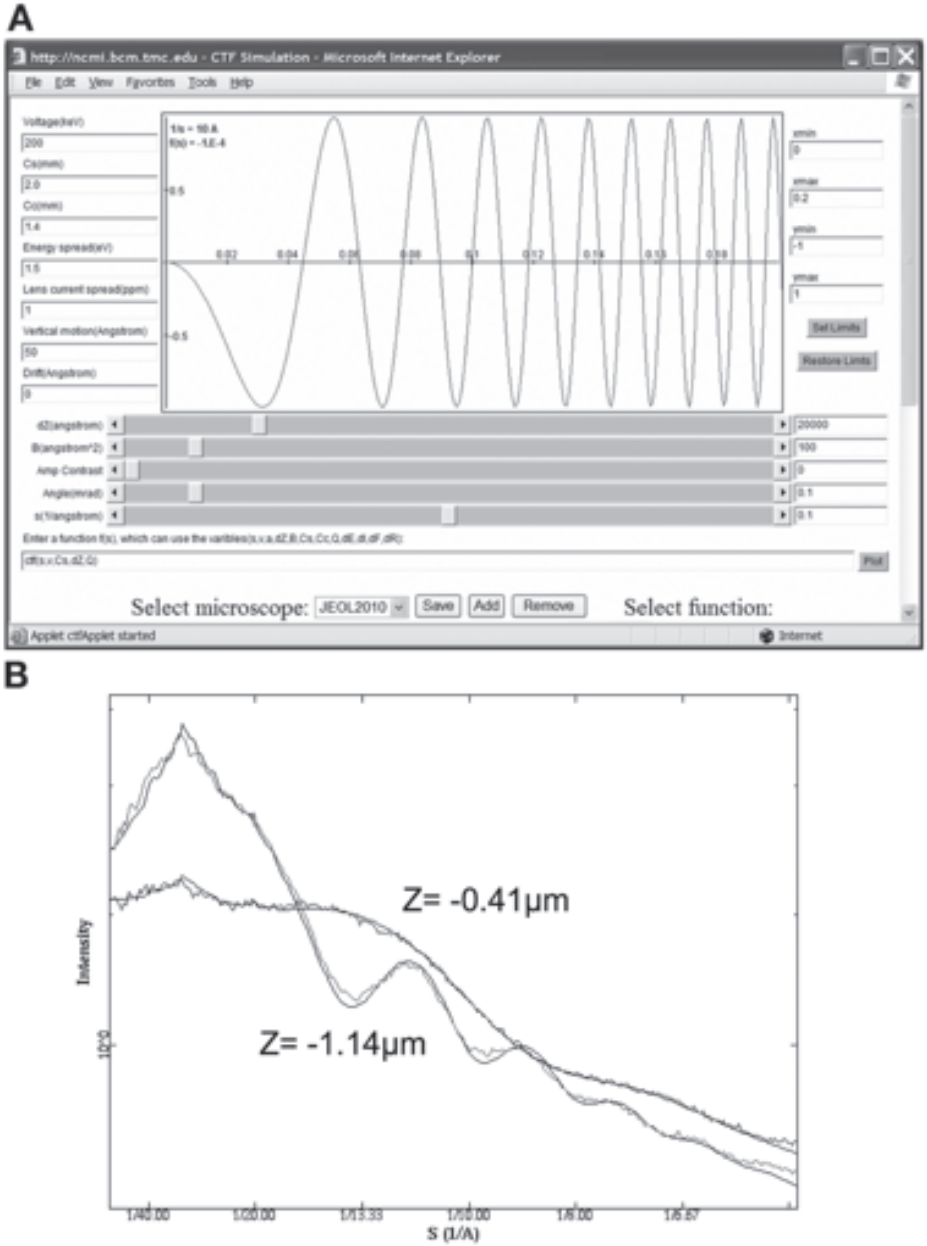

Fig. 4. Contrast transfer function. **(A)** Snapshot of the online CTF simulation (http://ncmi.bcm.edu/homes/wen/ctf). **(B)** Examples of good fits of contrast transfer function. Shown are two micrographs of rice dwarf virus imaged on a JEM4000 electron microscope with underfocuses of 0.41 μm and 1.14 μm, respectively.

(10) that can be used for these image processing steps. SAVR is a subset of programs within EMAN that has been developed based on Crowther's algorithm for icosahedral particle reconstruction. This method specifically takes advantage of the high symmetries of icosahedral viruses and is very efficient in computing. It is particularly useful for initial model building. Nevertheless, EMAN is a generic single particle image processing software package that also supports other symmetries in addition to performing icosahedral reconstruction. Adopting the generic single particle package, EMAN, offers additional benefits in that the same software can be used to determine structures of the non-icosahedral components in an icosahedral particle ***(36)***.

3.3.1. Build Initial Model

Several approaches can be used to generate the initial model. The first method is to use the *starticos* program that will find the images with best five-, three-, and twofold symmetry and build a low-resolution initial model from these images. The second method is simply using a synthetic icosahedron-shaped model that is roughly similar in size to the virus under investigation. The later step in EMAN refinement cycles are generally powerful enough to converge to the proper structure. The third method is to use the *buildim.py* in SAVR that relies on the self common-line method and Fourier-Bessel synthesis method.

3.3.2. 2D Alignment

2D alignment refers to the task that determines the five parameters for each particle image: three for rotational angles and two for particle center positions in 2D. Euler angles generally are used to represent the three rotational parameters (*see* **Note 5**).

In EMAN, many different 2D alignment algorithms are available, ranging from projection matching, common-lines, to principal component analysis. The projection matching method is the most mature and recommended approach for this step. In this method, an exhaustive collection of projections of the 3D model are first generated using the *project3d* program to cover the complete orientational asymmetric unit. Each particle is aligned to all the projections and the orientation of the best matched projection is assigned to the particle. This step is also often referred to as the classification step because each projection from the model serves as a reference to group the particles with similar orientations. This step is performed using the *classesbymra* program. Many similarity scoring functions, such as dot product, phase difference, integrated Fourier ring correlation, and linear least square difference, etc., are available. In general, the linear least square difference in combination with matched filter (option *dfilt*) is a good choice for the scoring function. After the orientations of all particles have been determined, the particles with the same orientations (i.e., assigned

to the same best matched projection) are averaged to generate a class average with improved signals over individual particles using the *classalignall* program.

Note that the 2D alignment by *classesbymra* simply ranks the similarity of each particle compared with all projection images. It does not decide which subsets of particles are "bad" or "good." The class averaging step by *classalignall* makes these decisions and excludes those "bad" particles in the final class averages. This step is performed by evaluating the similarities among the particles within the same class, building the similarity histogram, and discarding the particles with least similarities to other particles by using a user-selectable threshold (typically 1 sigma or less above mean specified using the *keep* option). Additionally, the particles with vastly different orientation assignments in different refinement iterations can be detected and removed using the program *ptcltrace* with *zap* option.

3.3.3. 3D Reconstruction

Once the orientations of each particle is determined and class averages are generated, a 3D reconstruction procedure will be performed to coherently merge the 2D class averages into a single 3D density map at the highest possible resolution allowed by the data. In EMAN, the *make3d* (*see* **Note 6**) program implementing the direct Fourier inversion method is the default reconstruction program. In this step, it is also possible to further remove the bad particle images by discarding the class averages that don't agree well with the reconstruction (using *hard* option).

3.3.4. CTF Correction

In EMAN, CTF correction is performed at two separate stages. After CTF determination, the 2D particle raw images are immediately phase-corrected using the graphic program *ctfit* or the command-line program *applyctf* before orientation determination. These two programs also record the CTF parameters in the image header of each particle for later CTF amplitude correction (*see* **Note 7**). The amplitude correction (using the *refine* program *ctfcw* option) is performed at the class averaging stage by using a Wiener filter and relative SNR weighting of contributions from different particles ***(10)***. A satisfactory CTF correction is critically dependent on accurate determination of the CTF and associated parameters, both defocus and amplitude decay factor, of the raw particle images. A useful visual criterion of proper CTF compensation is the absence of apparent black rings just outside of the particle images in the class averages.

3.3.5. Automated Image Refinement

The aforementioned tasks (2D alignment, class averaging, CTF correction, and 3D reconstruction) and the iteration of these tasks are automated by the

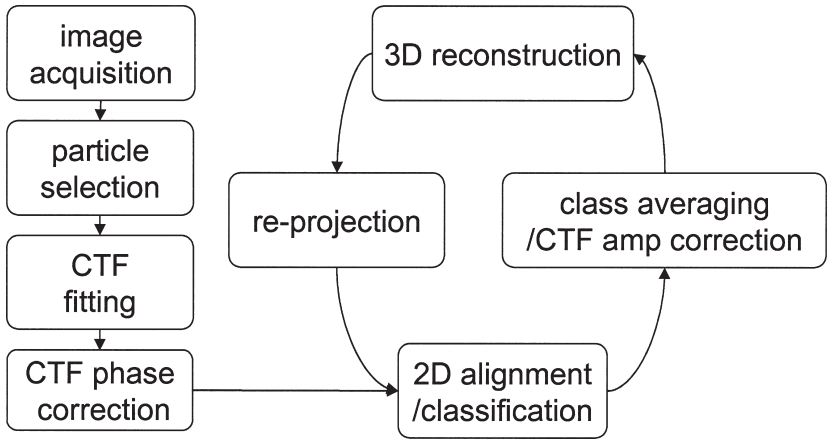

Fig. 5. Schematic diagram of the image processing for icosahedral particles using EMAN.

program *refine*. In the working directory, the phase-corrected raw particles should be pooled into a single image file named *start.hed/start.img* (*see* **Note 8**) with the CTF parameters embedded in the image headers of each particle. An initial model named *threed.0a.mrc* should also be placed in this directory. The structure factor file used for CTF determination should also be present (*see* **Note 4**). Then the *refine* command can be started to perform the iterative 3D map reprojection, orientation determination using projection matching, class averaging, CTF correction, and 3D reconstruction until convergence (*see* **Fig. 5**). A sample *refine* command is given here, which can be a good starting point to tailor to different data sets:

refine < number of iterations > sym=icos ang= < angular stepsize in degree for reprojection > mask= < mask radius in pixel > ctfcw= < structural factor filename > classkeep=1 classiter=3 dfilt refine proc= < number of CPU >

3.4. Structural Analysis

Once the 3D reconstruction refinement has converged, further structural analysis is necessary to segment out the individual subunits and examine their characteristic structural features.

3.4.1. Resolution Determination

The resolution of the 3D reconstruction is, in general, determined using the Fourier shell correlation (FSC) between two reconstructions that are generated using the half datasets ***(37)***. Different researchers all are in agreement about

the usage of FSC, differences among them exist regarding how it is performed, for instance, what stage the datasets should be split, what type of masking is legitimate, and what threshold to use to read the resolution from the FSC curve ***(38,39)***. In EMAN, the resolution evaluation is performed using program *eotest*, which splits each of the classes into halves and performs class averaging and 3D reconstruction by treating the two sets of classes as independent datasets. Before computing the FSC curve, the two 3D reconstructions were masked optionally using an adaptive auto-masking procedure (the *proc3d automask2* option) to remove the background noises without using fixed mask geometry to avoid artificially inflated correlation from the masks. From the FSC curve, we use the 0.5 criterion (the resolution where the FSC value falls to 0.5) as the reported resolution for the final 3D reconstruction. We feel that the resolution number determined this way matches best to the visible structural features especially when the secondary structural elements are resolved in the subnanometer resolution range (*see* **Note 9**).

3.4.2. Segmentation, Visualization, and Animation

Visualization and segmentation of the 3D density map are essential tasks to structural interpretation. Both commercial graphical softwares such as *IRIX Explorer*, *Amira*, and open source softwares such as *Chimera* and *pymol* can be used. In our experience, *Amira* currently has the best overall features, covering all needs of visualization and segmentation and is relatively easy to learn and use. Animations can also be easily created using *Amira*. Alternatively, *Chimera* is an excellent open source alternative especially for hybrid visualization of density maps and PDB atomic models. Preliminary animation capabilities in *Chimera* are also available as a plugin (*emanimator*) provided by EMAN.

The visualization and segmentation of large virus density maps at subnanometer resolutions is very demanding and requires a decent desktop computer or workstation with a good graphical card. A desktop computer equipped with >2GHz CPU, >1 GB memory, and a Nvidia GeForce 4 or later graphical card will be a good configuration.

For an icosahedral virus structure at subnanometer resolutions, typical segmentation tasks are to cut out the asymmetric unit and each of the composing subunits in this asymmetry unit. Subunit boundaries should be resolved at the majority of places except for areas where intimate interactions exist among neighboring subunits. These individual subunits were generally visualized as isosurface views with different colors in isolation or in the context of whole capsid. The whole capsids were also commonly visualized as isosurface views along its five-, three- or twofold symmetry axes, viewed from either outside or inside, often radially colored (*see* **Fig. 6**).

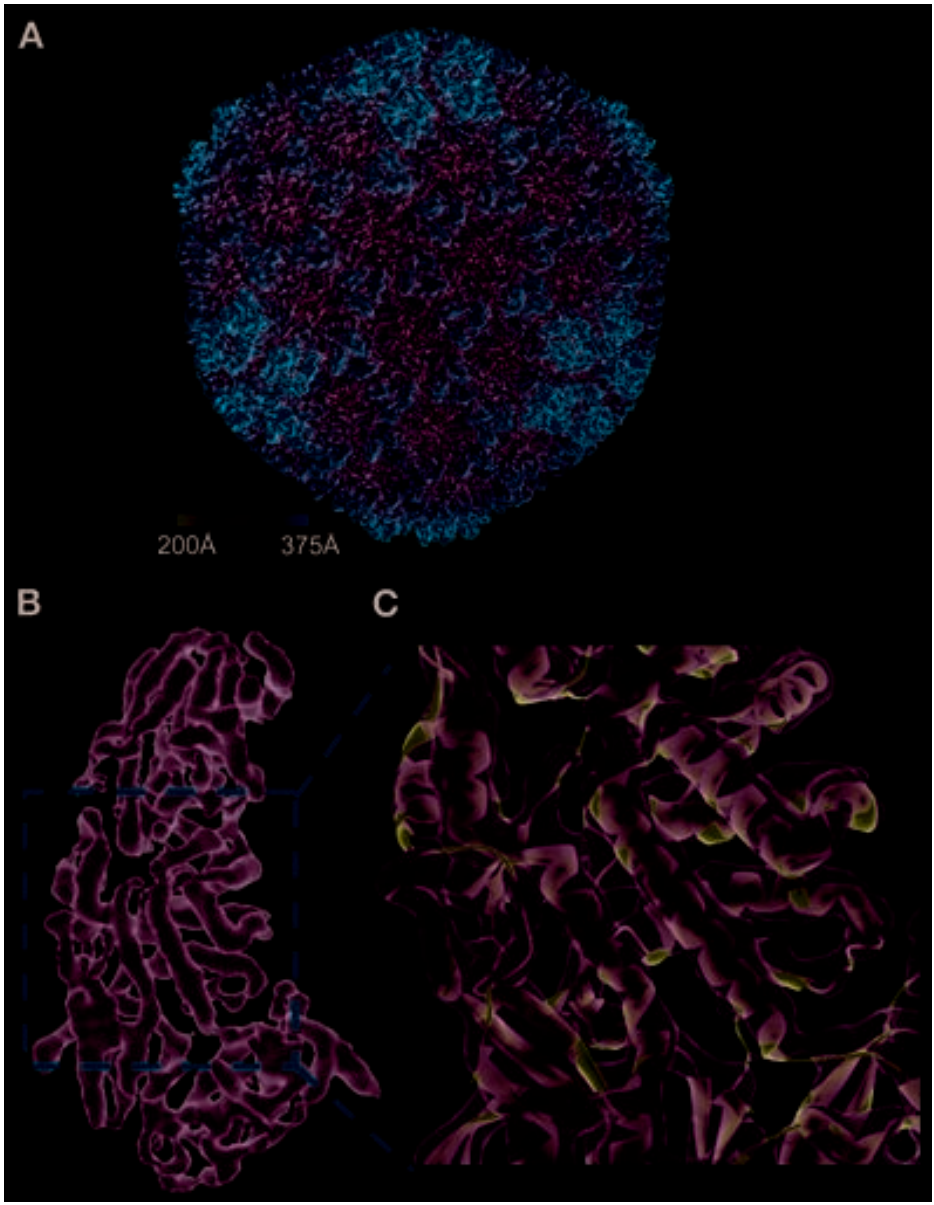

Fig. 6. Example of rice dwarf virus map at subnanometer resolution. **(A)** The whole capsid with radial coloring. **(B)** A single subunit of the inner shell protein P3b. **(C)** Zoomed view of the carapace domain of P3b with the superimposition of subsequently X-ray crystallographically determined model.

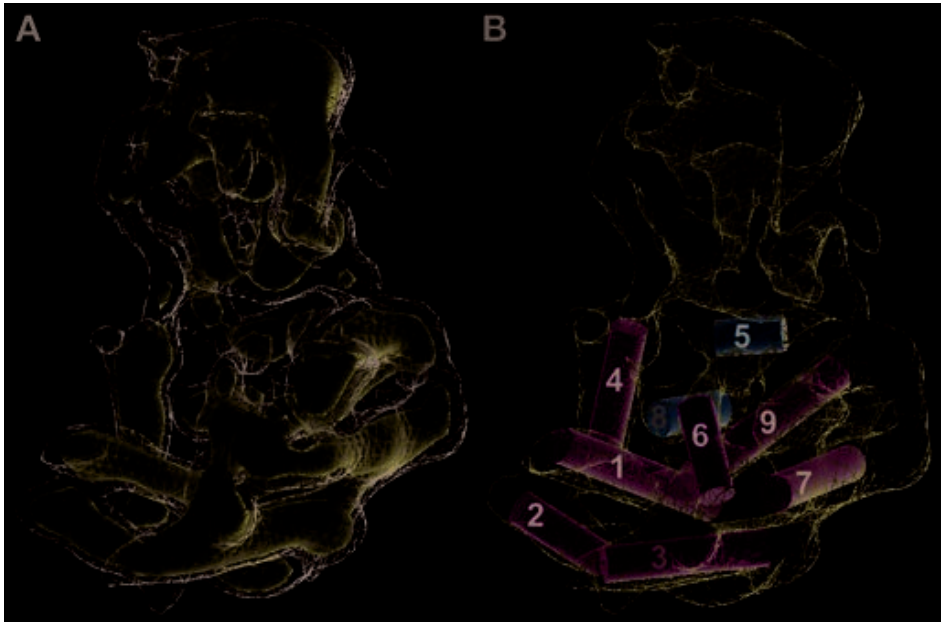

Fig. 7. Secondary structural elements identified in rice dwarf virus outer shell protein P8. **(A)** The average monomer subunit; **(B)** the identified 9 helices in the lower domain.

3.4.3. Identification of Secondary Structure Elements

At subnanometer resolutions, the alpha helices would appear as rod-like shapes of 5 to 6 Å diameter and varying lengths. The sheets are flat, smooth densities with varying curvatures. The helices and sheets can be visually identified by interactively examining the graphical display or through a more objective process using the programs *helixhunter* and *ssehunter* provided in EMAN ***(8)***. These processes have been used to correctly identify the majority of the SSEs in many 3D reconstructions at subnanometer resolutions ***(6,40,41)***. The identified SSEs encode rich information. The relative positions and orientations of these SSEs can uniquely represent the protein fold and can be used to search for homologue structures in the PDB. This procedure has been successfully employed to identify homologous protein folds for several virus capsid proteins and have lead to a substantially deeper understanding of the assembly principles of these virus capsids (*see* **Fig. 7,** and also **refs.** ***6,17,40,41***). In addition, direct visualization of secondary structure features is a good indicator whether a 3D reconstruction reaches truly subnanometer resolutions.

4. Notes

1. The blotting is a critical step that will ultimately decide if the resulting grid is usable. Insufficient blotting will result in too thick ice and over-blotting will leave a bare grid. Since the blotting task is to remove >99.9% (3–5 μL) of the solution and leave <0.1% (~1 nL) of the sample on the grid, it is extremely sensitive to the sample viscosity, grid surface hydrophobicity, environmental humidity, filter paper wetness, contact between the filter paper and grid, and the duration of the blotting. One should be prepared for the potential difficulties in this step, especially for sample buffers including glycerol/sucrose, detergent or high concentration of salt (1 *M*). Currently, there is no method that can guarantee the success of every blotting/freezing. Practice and experience through systematic trial-and-error is the only solution to get around the difficulties.
2. The cryotransfer process should be practiced very carefully and be performed rapidly and smoothly; it is essential to ensure minimal exposure to the room moisture and to avoid ice-contamination and excessive temperature increase of the grid.
3. The Nikon scanner records the transmittance rather than the optical density directly. A log transform is needed to convert the image values so that the values are linearly proportional to optical density for later image processing. Different image processing packages have different assumptions about the scanned image's contrast: some, such as EMAN, expect that the pixel values for the particles are larger than the values of background pixels, whereas others expect the opposite. The image contrast of CCD images and Z/I SCAI scanner images need to be inverted before proceeding to image processing using EMAN.
4. The structure factor curve of the imaged specimen is needed for a good fit of the CTF parameters. X-ray solution scattering experiments usually are used to acquire these curves ***(29)***. Alternatively, simultaneous fitting of multiple micrographs could be used (http://ncmi.bcm.edu/homes/stevel/EMAN/doc/faq.html).
5. There are many different conventions of Euler angles used in different software packages. The user must be very careful to convert the parameters properly if different software packages are used for one dataset. In EMAN, conversions among most of the Euler angle conventions and other representations of rotation (spin axis and quaternion) are supported.
6. *make3d* needs to hold four copies of the 3D reconstruction in memory. For large reconstructions, a 64bit computer with 4+ GB memory might be required for a reconstruction map larger than 600^3 pixels.
7. Currently, all particles in the same micrograph are treated to have the same CTF modulation and astigmatism is ignored by discarding apparently astigmatic micrographs.
8. The 2D particle images are typically in IMAGIC format or the special EMAN LST format. The LST format is a text file with links to the actual binary image files. It is especially useful when there are too many particles that cause the total IMAGIC format file size to exceed 2 GB, which is not supported properly on many computer systems. Multiple image files in IMAGIC format can be consolidated into a single LST file using the *lstcat.py* program.

9. The resolution number judged from FSC using any threshold criterion is just a rough estimate of the map quality, and it is somewhat sensitive to the exact masking and other operations before the curve is calculated. It is often true that different areas of the structure have different qualities mostly due to conformational variability. This type of quality variation is poorly represented by a single global resolution number. It is not an absolutely reliable quality ranking criterion for judging the quality or the correctness of the map.

Acknowledgments

We thank Joanita Jakana and Z. Hong Zhou for the RDV images used in the figures. The research has been supported by NIH grants P41RR02250, R01GM 070557, R01AI38469, the Agouron Institute and the Robert Welch Foundation.

References

1. Crowther, R. A., Amos, L. A., Finch, J. T., De Rosier, D. J., and Klug, A. (1970) Three dimensional reconstructions of spherical viruses by fourier synthesis from electron micrographs. *Nature* **226,** 421–425.
2. Crowther, R. A. (1971) Procedures for three-dimensional reconstruction of spherical viruses by fourier synthesis from electron micrographs. *Phil. Trans. Roy. Soc. Lond. B.* **261,** 221–230.
3. Bottcher, B., Wynne, S. A., and Crowther, R. A. (1997) Determination of the fold of the core protein of hepatitis B virus by electron cryomicroscopy. *Nature* **386,** 88–91.
4. Conway, J. F., Cheng, N., Zlotnick, A., Wingfield, P. T., Stahl, S. J., and Steven, A. C. (1997) Visualization of a 4-helix bundle in the hepatitis B virus capsid by cryo-electron microscopy. *Nature* **386,** 91–94.
5. Zhou, Z. H., Dougherty, M., Jakana, J., He, J., Rixon, F. J., and Chiu, W. (2000) Seeing the herpesvirus capsid at 8.5 Å. *Science* **288,** 877–880.
6. Zhou, Z. H., Baker, M. L., Jiang, W., Dougherty, M., Jakana, J., Dong, G., Lu, G., and Chiu, W. (2001) Electron cryomicroscopy and bioinformatics suggest protein fold models for rice dwarf virus. *Nat. Struct. Biol.* **8,** 868–873.
7. Chiu, W., Baker, M. L., Jiang, W., Dougherty, M., and Schmid, M. F. (2005) Electron cryomicroscopy of biological machines at subnanometer resolution. *Structure* **13,** 363–372.
8. Jiang, W., Baker, M. L., Ludtke, S. J., and Chiu, W. (2001) Bridging the information gap: computational tools for intermediate resolution structure interpretation. *J. Mol. Biol.* **308,** 1033–1044.
9. Chiu, W., Baker, M. L., Jiang, W., and Zhou, Z. H. (2002) Deriving folds of macromolecular complexes through electron cryomicroscopy and bioinformatics approaches. *Curr. Opin. Struct. Biol.* **12,** 263–269.
10. Ludtke, S. J., Baldwin, P. R., and Chiu, W. (1999) EMAN: semiautomated software for high-resolution single-particle reconstructions. *J. Struct. Biol.* **128,** 82–97.

11. Jiang, W., Li, Z., Zhang, Z., Booth, C. R., Baker, M. L., and Chiu, W. (2001) Semi-automated icosahedral particle reconstruction at sub-nanometer resolution. *J. Struct. Biol*. **136,** 214–225.
12. Good, N. E., Winget, G. D., Winter, W., Connolly, T. N., Izawa, S., and Singh, R. M. (1966) Hydrogen ion buffers for biological research. *Biochemistry* **5,** 467–477.
13. Adrian, M., Dubochet, J., Lepault, J., and McDowall, A. W. (1984) Cryo-electron microscopy of viruses. *Nature* **308,** 32–36.
14. Dubochet, J., Adrian, M., Chang, J. J., et al. (1988) Cryo-electron microscopy of vitrified specimens. *Q. Rev. Biophys.* **21,** 129–228.
15. Fukami, A. and Adachi, K. (1965) A new method of preparation of a self-perforated micro plastic grid and its application. *J. Electron Microsc.* **14,** 112–118.
16. Jeng, T. W., Talmon, Y., and Chiu, W. (1988) Containment system for the preparation of vitrified-hydrated virus specimens. *J. Electron Microsc. Tech.* **8,** 343–348.
17. Booth, C. R., Jiang, W., Baker, M. L., Zhou, Z. H., Ludtke, S. J., and Chiu, W. (2004) A 9 Å single particle reconstruction from CCD captured images on a 200 kV electron cryomicroscope. *J. Struct. Biol*. **147,** 116–127.
18. Suloway, C., Pulokas, J., Fellmann, D., et al. (2005) Automated molecular microscopy: the new Leginon system. *J. Struct. Biol.* **151,** 41–60.
19. Zhang, P., Beatty, A., Milne, J. L., and Subramaniam, S. (2001) Automated data collection with a Tecnai 12 electron microscope: applications for molecular imaging by cryomicroscopy. *J. Struct. Biol.* **135,** 251–261.
20. Lei, J. and Frank, J. (2005) Automated acquisition of cryo-electron micrographs for single particle reconstruction on an FEI Tecnai electron microscope. *J. Struct. Biol.* **150,** 69–80.
21. Saban, S. D., Nepomuceno, R. R., Gritton, L. D., Nemerow, G. R., and Stewart, P. L. (2005) CryoEM structure at 9 Å resolution of an adenovirus vector targeted to hematopoietic cells. *J. Mol. Biol.* **349,** 526–537.
22. Ludtke, S. J., Chen, D. H., Song, J. L., Chuang, D. T., and Chiu, W. (2004) Seeing GroEL at 6 Å resolution by single particle electron cryomicroscopy. *Structure* **12,** 1129–1136.
23. Jiang, W., Baker, M. L., Wu, Q., Bajaj, C., and Chiu, W. (2003) Applications of a bilateral denoising filter in biological electron microscopy. *J. Struct. Biol.* **144,** 114–122.
24. Zhu, Y., Carragher, B., Glaeser, R. M., et al. (2004) Automatic particle selection: results of a comparative study. *J. Struct. Biol*. **145,** 3–14.
25. Kivioja, T., Ravantti, J., Verkhovsky, A., Ukkonen, E., and Bamford, D. (2000) Local average intensity-based method for identifying spherical particles in electron micrographs. *J. Struct. Biol*. **131,** 126–134.
26. Thon, F. (1971) Phase contrast electron microscopy, in *Electron Microscopy in Material Sciences* (Valdre, U., ed.), Academic Press, New York, pp. 571–625.
27. Erickson, H. P. and Klug, A. (1971) Measurement and compensation of de-focusing and aberrations by Fourier processing of electron micrographs. *Phil. Trans. Roy. Soc. Lond. B.* **261,** 105–118.

28. Hanszen, K. J. (1967) New knowledge on resolution and contrast in the electron microscope image. *Naturwissenschaften* **54,** 125–133.
29. Saad, A., Ludtke, S. J., Jakana, J., Rixon, F. J., Tsuruta, H., and Chiu, W. (2001) Fourier amplitude decay of electron cryomicroscopic images of single particles and effects on structure determination. *J. Struct. Biol.* **133,** 32–42.
30. Frank, J., Radermacher, M., Penczek, P., et al. (1996) SPIDER and WEB: processing and visualization of images in 3D electron microscopy and related fields. *J. Struct. Biol.* **116,** 190–199.
31. van Heel, M., Harauz, G., Orlova, E. V., Schmidt, R., and Schatz, M. (1996) A new generation of the IMAGIC image processing system. *J. Struct. Biol.* **116,** 17–24.
32. Grigorieff, N. (1998) Three-dimensional structure of bovine NADH:ubiquinone oxidoreductase (complex I) at 22 Å in ice. *J. Mol. Biol*. **277,** 1033–1046.
33. Baker, T. S. and Cheng, R. H. (1996) A model-based approach for determining orientations of biological macromolecules imaged by cryoelectron microscopy. *J. Struct. Biol*. **116,** 120–130.
34. Sorzano, C. O., Marabini, R., Velazquez-Muriel, J., et al. (2004) XMIPP: a new generation of an open-source image processing package for electron microscopy. *J. Struct. Biol.* **148,** 194–204.
35. Liang, Y., Ke, E. Y., and Zhou, Z. H. (2002) IMIRS: a high-resolution 3D reconstruction package integrated with a relational image database. *J. Struct. Biol.* **137,** 292–304.
36. Jiang, W., Chang, J., Jakana, J., Weigele, P., King, J., and Chiu, W. (2006) Structure of Epsilon15 phage reveals organization of genome and DNA packaging/injection apparatus. *Nature* **439,** 612–616.
37. Harauz, G. and van Heel, M. (1986) Exact filters for general geometry three dimensional reconstruction. *Optik* **73,** 146–156.
38. van Heel, M. and Schatz, M. (2005) Fourier shell correlation threshold criteria. *J. Struct. Biol*. **151,** 250–262.
39. Rosenthal, P. B. and Henderson, R. (2003) Optimal determination of particle orientation, absolute hand, and contrast loss in single-particle electron cryomicroscopy. *J. Mol. Biol.* **333,** 721–745.
40. Baker, M. L., Jiang, W., Bowman, B. R., et al. (2003) Architecture of the herpes simplex virus major capsid protein derived from structural bioinformatics. *J. Mol. Biol*. **331,** 447–456.
41. Jiang, W., Li, Z., Zhang, Z., Baker, M. L., Prevelige, P. E., Jr., and Chiu, W. (2003) Coat protein fold and maturation transition of bacteriophage P22 seen at subnanometer resolutions. *Nat. Struct. Biol*. **10,** 131–135.